ELSEVIER

Journal of Hydrology 212–213 (1998) 198–212

Journal of Hydrology

A remote sensing surface energy balance algorithm for land (SEBAL)
1. Formulation

W.G.M. Bastiaanssen[a,*], M. Menenti[a], R.A. Feddes[b], A.A.M. Holtslag[c]

[a]*DLO-The Winand Staring Center for Integrated Land, Soil and Water Research, P.O. Box 125, 6700 AC Wageningen, The Netherlands*
[b]*Agricultural University Wageningen, Department of Water Resources, Nieuwe Kanaal 11, 6709 PA Wageningen, The Netherlands*
[c]*Royal Netherlands Meteorological Institute/Institute of Maritime and Atmospheric Research, P.O. Box 201, 3730 AE De Bilt, The Netherlands*

Abstract

The major bottlenecks of existing algorithms to estimate the spatially distributed surface energy balance in composite terrain by means of remote sensing data are briefly summarised. The relationship between visible and thermal infrared spectral radiances of areas with a sufficiently large hydrological contrast (dry and wet land surface types, vegetative cover is not essential) constitute the basis for the formulation of the new Surface Energy Balance Algorithm for Land (SEBAL). The new algorithm (i) estimates the spatial variation of most essential hydro-meteorological parameters empirically, (ii) requires only field information on short wave atmospheric transmittance, surface temperature and vegetation height, (iii) does not involve numerical simulation models, (iv) calculates the fluxes independently from land cover and (v) can handle thermal infrared images at resolutions between a few meters to a few kilometers. The empirical relationships are adjusted to different geographical regions and time of image acquisition. Actual satellite data is inserted in the derivation of the regression coefficients. Part 2 deals with the validation of SEBAL.

Keywords: Surface energy balance; Evaporation; Remote sensing

1. Introduction

c:/autopag/out/Land surface processes are of paramount importance for the re-distribution of moisture and heat in soil and atmosphere. The exchanges of radiative, heat and moisture fluxes affect the biosphere development and physical living conditions on earth. The thermo-dynamic equilibrium between turbulent transport processes in the atmosphere and laminar processes in the sub-surface manifests itself in the land surface energy balance, which reads as

$$Q^* = G_0 + H + \lambda E \qquad (\mathrm{Wm}^{-2}), \tag{1}$$

Where Q^* is net radiation, $G_0$is soil heat flux, H is sensible heat flux and λE is latent heat flux. The sign convention of Eq. (1) is that Q^* is considered positive when radiation is directed towards the surface, while G_0, H and λE are considered positive when directed away from the land surface. Eq. (1) neglects the energy required for photosynthesis and the heat storage in vegetation. Time integrated values of latent heat flux, λE, are important for different applications in hydrology, agronomy and meteorology. Numerical models for crop growth (e.g. Bouman et al., 1996), watersheds (e.g. Famigliette and Wood, 1994), river basins (e.g. Kite et al., 1994) and climate hydrology (e.g. Sellers et al., 1996) can contribute to an improved future planning and management of land

* Corresponding author. Corresponding address. ITC, P.O. Box 6, 7500 AA Enschede, The Netherlands.

0022-1694/98/$ - see front matter
PII: S0022-1694(98)00253-4

and water resources. The number of these distributed hydrological models and land surface parameterization schemes for climate studies is still growing, while research on techniques as to how to verify model predicted energy balances and evaporation at the landscape and continental scale remains an underestimated issue. Hence, a serious question in regional evaporation studies needs to be addressed: *How can regional evaporation predicted by simulation models be validated with limited field data and can remote sensing help this verification process?*

Remote sensing data provided by satellites are a means of obtaining consistent and frequent observation of spectral reflectance and emittance of radiation of the land surface on micro to macro scale. Overviews on retrieving evaporation from these spectral radiance's have been presented by Choudhury (1989); Schmugge (1991); Moran and Jackson (1991); Menenti (1993); Kustas and Norman (1996) and Bastiaanssen (1998). Classical remote sensing flux algorithms based on surface temperature measurements in combination with spatially constant other hydro-meteorological parameters may be suitable for assessing the surface fluxes on micro scale (e.g. Jackson et al., 1977), but not for meso and macro scale. Hence, more advanced algorithms have to be designed for composite terrain at a larger scale with physio-graphically different landscapes. Most current remote sensing flux algorithms are unsatisfactory to deal with practical hydrological studies in heterogeneous watersheds and river basins, because of the following common problems:

- As a result of spatial variations in land use, land cover, soil physical properties and inflow of water, most hydro-meteorological parameters exhibit an evident spatial variation, which cannot be obtained from a limited number of synoptic observations.
- Availability of distributed in-situ measurements of solar radiation, air temperature, relative humidity and wind speed during satellite overpass is restricted. Some remote sensing flux algorithms require reference surface fluxes which are only measured during dedicated field studies.
- The performance of remote sensing flux algorithms in heterogeneous terrain is difficult to quantify. Large scale experimental studies towards the area-effective surface energy balances fail even with 20 flux stations to assess the distributed and area-effective fluxes (e.g. Pelgrum and Bastiaanssen, 1996).
- Remote sensing observations provide basically an instantaneous 'snapshot' of the radiative properties of the land surface. A general framework to justify a daytime integration of surface fluxes from instantaneous observations is usually lacking.
- The required accuracy of aerodynamic surface temperature ($\pm$ 0.5 K) to calculate the sensible heat flux from remotely sensed radiometric surface temperature and synoptic air temperature can hardly be met (e.g.Brutsaert et al., 1993).
- A proper quantification of the surface roughness for heat transport from the surface roughness for momentum transport seems only feasible if supported by local calibrations (e.g. Blyth and Dolman, 1995). This correction is required for converting the remotely sensed radiometric surface temperature to aerodynamic temperature (e.g. Norman and Becker, 1995; Troufleau et al., 1997).
- The spatial scales of remote sensing measurements do not necessarily commensurate with those of the processes governing surface fluxes (e.g. Moran et al., 1997).
- Intra-patch advection cannot be accounted for as the surface fluxes are schematised to be vertical.
- Several remote sensing algorithms are often used in conjunction with data demanding hydrological and Planetary Boundary Layer models, which makes an operational application at regional scales cumbersome (e.g. Taconet et al., 1986; Choudhury and DiGirolamo, 1998).
- Information on land use types for the conversion between surface temperature to an expression of latent heat flux (e.g. Nieuwenhuis et al., 1985;Sucksdorff and Ottle, 1990) or for the ascription of hydro-meteoroglogical parameters (e.g. Taylor et al., 1997) are sometimes required. These methods are less suitable for sparse canopies and landscapes with an irregular geometry and complex structure.

To overcome most of these problems, a physically based 'multi-step' Surface Energy Balance Algorithm for Land (SEBAL) has been formulated (Bastiaanssen, 1995). SEBAL uses surface temperature T_0, hemispherical surface reflectance, r_0 and Normalized

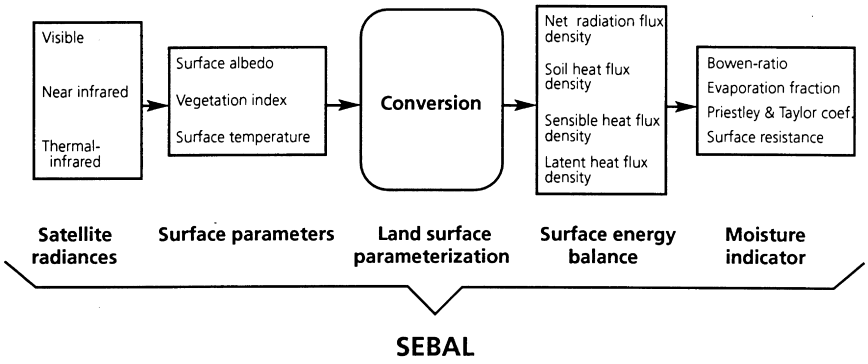

Fig. 1. Principal components of the Surface Energy Balance Algorithm for Land (SEBAL) which converts remotely measured spectrally emitted and reflected radiance's into the surface energy balance and land wetness indicators.

Difference Vegetation Index (NDVI), as well as their interrelationships to infer surface fluxes for a wide spectrum of land types. A conceptual scheme of SEBAL is presented in Fig. 1. SEBAL describes λE as the rest term of the instantaneous surface energy balance, λE

$$\lambda E(x,y) = F_1\{r_0(x,y), K^{\downarrow}(x,y), \varepsilon_2', \varepsilon_0(x,y), \times T_0(x,y), G_0(x,y), Z_{0m}(x,y), kB^{-1}, \times u_*(x,y), L(x,y), \delta T_a(x,y)\}, \quad (2)$$

Where r_0 is the hemispherical surface reflectance, $K^{\downarrow}$ (Wm^{-2}) is the incoming solar radiation, ε_2' is the apparent thermal infrared emissivity of the atmosphere, ϵ_0 is the surface thermal infrared emissivity, T_0(K) is the radiometric surface temperature, G_0(Wm^{-2}) the soil heat flux, z_{0m}(m) the surface roughness length for momentum transport, kB^{-1} the relationship between z_{0m} and the surface roughness length for heat transport, u_*(ms^{-1}) the friction velocity, L(m) the Monin–Obukhov length and δT_a(K) is the near-surface vertical air temperature difference. The (x,y) notation denotes that a particular parameter is variable in the horizontal space domain with a resolution of one pixel. The parameter is considered to be spatially constant if the (x,y) notation is not mentioned explicitly.

2. Atmospheric corrections

2.1. Hemispherical surface reflectance, $r_0(x,y)$

Registrations of in-band reflected radiation at the top of atmosphere $K^{\uparrow}_{TOA}$(b) by operational earth observation satellites are usually acquired from a single direction. Corrections for atmospheric interference are generally based on detailed information on the state of the atmosphere (temperature, humidity and wind velocity at different altitudes), as extracted from radiosoundings. If this data is not available, the hemispherical surface reflectance r_0 may be obtained from the broadband directional planetary reflectance r_p in a simple and straightforward manner (Chen and Ohring, 1984; Koepke et al., 1985)

$$r_0 = \frac{r_p - r_a}{\tau_{sw}''}, \quad (3)$$

where r_a is the fractional path radiance and τ_{sw}'' is the two-way transmittance. The surface albedo r_0 of the darkest pixel (e.g. deep sea) may be zero. If $r_0 = 0$, it follows from Eq. (3) that r_a is equal to r_p of a deep sea or any other dark target. Pyranometer measurements of $K^{\downarrow}$ can be used to derive the single way transmittance τ_{sw} from $K^{\downarrow}$ and extra-terrestrial radiation from which the two-way transmittance $\tau_{sw}''(\tau_{sw}'' = \tau_{sw}^{*}\tau_{sw})$ can be assessed. The average error in estimating r_0 from r_p through Eq. (3) is $\Delta r_0 = 0.04$ (Bastiaanssen, 1998).

2.2. Land surface temperature, $T_0(x,y)$

Long wave radiation can only be transmitted through the atmosphere in those ranges of the spectrum, where the molecular absorption by water vapour, gases and suspended materials is minimized, i.e. the atmospheric windows. Thermal infrared radio-

meters have narrow bands in parts of the 8–14 μm spectrum coinciding with these atmospheric windows. The relationship between the in-band spectral long wave radiance $L^{\uparrow}_{\mathrm{TOA}}(\mathrm{b})$ measured by spaceborne thermal infrared radiometers and the at-surface value $L^{\uparrow}(\mathrm{b})$ in the same spectral interval for a homogeneous atmosphere reads as

$$L^{\uparrow}_{\mathrm{TOA}}(\mathrm{b},x,y) = \tau_{\mathrm{lw}}(\mathrm{b})L^{\uparrow}(\mathrm{b},x,y) + L^{\uparrow}_{\mathrm{atm}}(\mathrm{b}) + \tau_{\mathrm{lw}}(\mathrm{b})(1 - \varepsilon_0(\mathrm{b},x,y))L^{\downarrow}(\mathrm{b}) \qquad (\mathrm{Wm}^{-2}), \quad (4)$$

where $L^{\uparrow}_{\mathrm{atm}}(\mathrm{b})$ is the upward emitted sky radiation (thermal path radiance), $\tau_{\mathrm{lw}}(\mathrm{b})$ represents the atmospheric transmittance applicable in the region b, $L^{\downarrow}(\mathrm{b})$ is the downwelling thermal radiance in the region b owing to atmospheric emittance and ϵ_0 is the thermal infrared surface emissivity. The absence of accurate data on the atmospheric composition which can be used to compute $L^{\uparrow}_{\mathrm{atm}}(\mathrm{b})$ and $\tau_{\mathrm{lw}}(\mathrm{b})$ at the moment of satellite overpass must be considered a norm, rather than an exception. It is therefore, proposed to derive $\tau_{\mathrm{lw}}(\mathrm{b})$ and $L^{\uparrow}_{\mathrm{atm}}(\mathrm{b})$ from a regression analysis between $L^{\uparrow}_{\mathrm{TOA}}(\mathrm{b})$ measured at the satellite and in situ $L^{\uparrow}(\mathrm{b})$ values, where $L^{\uparrow}(\mathrm{b})$ is computed from radiometric surface temperature T_0 applying Planck's law in the region b.

3. Net radiation

Net radiation $Q^*(x,y)$ is calculated from the incoming and outgoing all wave radiation fluxes

$$Q^*(x,y) = (1 - r_0(x,y))K^{\downarrow}(x,y) + L^{\downarrow} - L^{\uparrow} \qquad (x,y) \qquad \mathrm{Wm}^{-2}, \quad (5)$$

where $L^{\downarrow}$ is the downwelling long wave radiation and $L^{\downarrow}(x,y)$ is the upwelling long wave radiation. As SEBAL is only meant for cloud free conditions, techniques to assess the degree of cloudiness from remote sensing measurements are not included in the list of equations provided with Appendix A. Solar radiation $K^{\downarrow}$ is computed according to the zenith angle of each individual pixel and therefore spatially variable, $K^{\downarrow}(x,y)$. Most natural surfaces do not emit longwave radiation as a black radiator. Van de Griend and Owe (1992) used an emissivity box together with radiometers to measure simultaneously NDVI and surface thermal infrared $\epsilon_0$in the savannah environment of Botswana. An emissivity ϵ_0 for the 8–14 μm spectral range could be predicted from NDVI using

$$\varepsilon_0(x,y) = 1.009 + 0.047 \ln \mathrm{NDVI}(x,y). \quad (6)$$

The application of Eq. (6) is restricted to measurements conducted in the range of NDVI = 0.16 − 0.74. The value for $\epsilon_0(x,y)$ can be used to calculate broad band grey body $L^{\uparrow}$ values from T_0, applying Stefan Boltzmann's law.

4. Soil heat flux

Many studies have shown that the midday G_0/Q^* fraction is highly predictable from remote sensing determinants of vegetation characteristics such as vegetation indices and LAI (see Daughtry et al., 1990, for a review). The G_0/Q^* approach fails, however, in sparse canopies, because heat transfer into the soil is becoming a more significant part of the net radiation if soils are bare and dry. An improved version of G_0/Q^* based on radiometric surface temperature T_0 is therefore proposed later. Another aspect which needs attention is the phase difference between G_0 and Q^* arising from soil thermal storage during a daytime cycle.

As Q^* can be mapped aerially on the basis of space borne $K^{\uparrow}(x,y)$ and $L^{\uparrow}(x,y)$ data, the G_0/Q^* fraction is an attractive tool to describe the regional G_0-patterns. Eq. (7) is obtained by combining the transfer equation for soil heat flux G_0 with the radiation balance (Eq. 5), and is expressed as a G_0/Q^* fraction

$$\Gamma = \frac{G_0}{Q^*} = \frac{\lambda_s(T_0 - T_s)}{z\{(1r_0)K^{\downarrow} + L^*\}}, \quad (7)$$

Where z (m) is the depth at which soil temperature T_s is measured (a few centimeters below the surface), λ_s ($\mathrm{Wm}^{-1}\,\mathrm{K}^{-1}$) is the apparent soil thermal conductivity and L^* (Wm^2) is the net long wave radiation ($L^{\downarrow} - L^{\uparrow}$). The mathematical shape of Eq. (7) shows that Γ increases with T_0 and r_0. Choudhury et al., (1984) introduced a *proportionality factor* Γ' to describe the conductive heat transfer in soil and an *extinction factor* Γ'' to describe the attenuation of radiation through canopies. Bare soils have an extinction factor of $\Gamma'' = 1.0$. For mixed vegetation, the

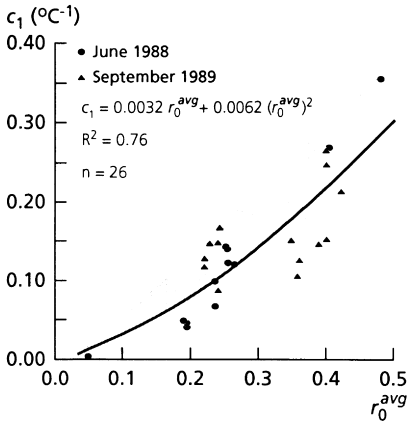

Fig. 2. Correlation between a factor c_1 (Eq. 10) and the daytime-average hemispherical surface reflectance r_0^{avg} on the basis of field measurements at different types of sebkha collected during the summer and fall of 1988 and 1989 respectively in the Qattara Depression, Western Desert of Egypt.

parameterization of Γ consists of the product of these two components:

$$\Gamma = \frac{G_0}{Q^*} = \Gamma' \Gamma''. \tag{8}$$

Field studies from the Qattara Depression in the Western Desert of Egypt, where vegetation is completely absent (thus $\Gamma'' = 1.0$), were applied to investigate the relationship between Q^*, G_0, T_0 and r_0. The daylight averaged G_0/Q^* values for the Qattara Depression were found to range from 0.092 to 0.355, and variations could be explained to top-soil moisture and solar positions.

As a result of the thermal storage in the top-soil and transient soil temperatures, the behaviour of Γ' undergoes a diurnal cycle, i.e. $\Gamma'(t)$. The best fit between the remotely sensed $T_0(t)$ and $r_0(t)$ parameters and field observed $\Gamma'(t)$ values becomes, according to the proportionality ascertained in Eq. (7), as follows:

$$\Gamma'(t) = \frac{T_0(t)}{r_0(t)} C_1. \tag{9}$$

where $T_0(t)$ is the surface temperature in degrees centigrade and $r_0(t)$ is the fractional hemispheric surface reflectance. The $T_0(t)/r_0(t)$ ratio in Eq. (9) describes the heat storage and heat release effects on $\Gamma'(t)$. The regression coefficient c_1 varies with soil properties and moisture (Fig. 2)

$$c_1 = 0.0032\, r_0^{avg} + 0.0062 (r_0^{avg})^2. \tag{10}$$

The daytime-representative value r_0^{avg} reflects colour as well as soil moisture conditions because wet bare soil surfaces have low r_0^{avg}-values and are characterised by low c_1 and $\Gamma'(t)$ values.

Soil underneath vegetation receives less radiation than bare soil, so $T_0 - T_s$ in Eq. (7) will be small. Information to describe $T_0 - T_s$ is not available for regional energy balance studies. Efforts to formulate Γ'' should therefore focus on remotely measurable vegetation parameters which control the attenuation of radiation. Choudhury (1989) showed that the extinction coefficient Γ'' decreases non-linearly with increasing soil cover and LAI. Kustas and Daughtry (1990) found a linear relationship between Γ'' and NDVI. In SEBAL, the NDVI was selected to describe

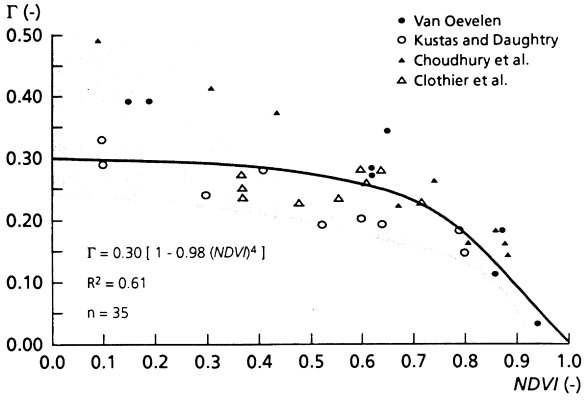

Fig. 3. Soil heat flux/net radiation data for a variety of surface types and soil cover as derived from Clothier et al. (1986), Choudhury (1989), Kustas and Daughtry (1990) and Van Oevelen (1993) to describe extinction effects by means of NDVI.

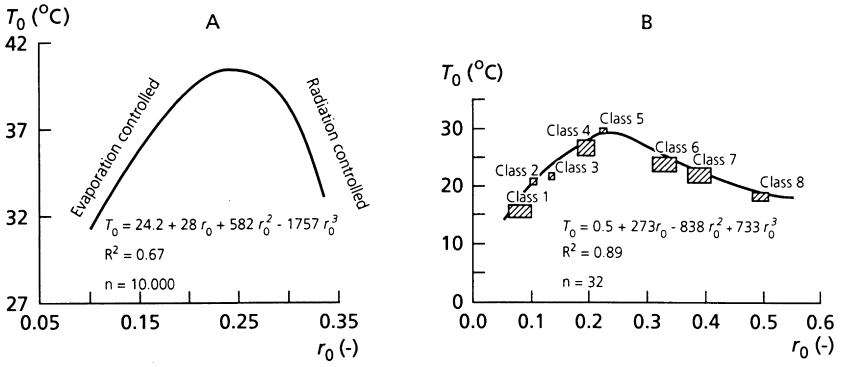

Fig. 4. Observed relationships between instantaneous surface temperatures, T_0, and hemispherical surface reflectance's, r_0, derived from Thematic Mapper measurements. Part A: Eastern Qattara Depression, path/row 178/39 acquired on 7 August, 1986, Part B: Western Qattara Depression, path/row 179/39, acquired on 13 November 1987.

the general effect of vegetation on surface fluxes see Fig. 1). Data from Clothier et al. (1986), Choudhury (1989), Kustas and Daughtry (1990) and van Oevelen (1991) shows that the best fit between Γ''and NDVI is

$$\Gamma'' = 1 - 0.978\,\mathrm{NDVI}^4. \tag{11}$$

As Γ gets gradually more affected by Γ′ when canopies become sparser (less attenuation by vegetation, which results in warmer soil pockets), the Γ-scatter within the envelope of Fig. 3 at low NDVI values increases. Combining Eqs. (8)–(11) gives the opportunity to describe the $G_0(Q^*)$ relationship for a wide spectrum of soil and canopy conditions

$$\Gamma'$$

$$\Gamma''\Gamma(t) = \frac{T_0(t)}{r_0(t)}\{0.0032\,r_0^{\mathrm{avg}} + 0.0062\,r_0^{\mathrm{avg2}}\} \times \{1 - 0.978(\mathrm{NDVI})^4\}. \tag{12}$$

5. Momentum flux

The relationship between momentum σ, sensible H and latent λE heat fluxes can be demonstrated easily by:

$$\sigma = \rho_a u_*^2 \qquad (\mathrm{Nm}^{-2}), \tag{13}$$

$$H = -\rho_a c_p u_* T_* \qquad (\mathrm{Wm}^{-2}), \tag{14}$$

$$\lambda = -\rho_a c_p u_* q_* \qquad (\mathrm{Wm}^{-2}), \tag{15}$$

where ρ_a (kg m^{-3}) is the moist air density, c_p (J kg^{-1} K^{-1}) the air specific heat at constant pressure, u_*(ms^{-1}) the friction velocity, T^* (K) the temperature scale and q^* the humidity scale. Appendix B elaborates the computation of the momentum flux in a tabular format.

5.1. Area-effective momentum flux

Classically, u_* is derived from wind profiles or sonic anemometers. Parts of a new method to determine the area-effective u_* from the negative slope between r_0 and T_0 was worked out by Menenti et al. (1989) Fig. 4 depicts measurements of $T_0(r_0)$ relationships made by Landsat Thematic Mapper during two different overpasses of the Qattara Depression in the Western Desert of Egypt. Diversity in surface hydrological conditions generates a wide range of (T_0,r_0)-values. The dry areas (sand dunes and limestone plateaux; groundwater is deep) have the largest reflectance ($r_0 = 0.220 - 0.30$) and contains the warmest spots with $T_0 = 312$–320 K at the moment of acquisition (see Fig. 4A). The coldest land surface elements with $r_0 = 0.10$ and $T_0 = 302$ K are marsh lands. According to Fig. 4, a positive correlation exhibits between T_0 and r_0 on wet to intermediately dry land ($r_0 < 0.23$ $T_0 < 313$ K, i.e. the *evaporation controlled branch*), whereas the relationship turns to negative when $r_0 > 0.23$, i.e. the *radiation controlled branch*. Similar relationships, but for a different range of T_0 according to prevailing weather conditions, have been found in other climates and landscapes (e.g. Seguin et

al., 1989; Rosema and Fiselier (1990). The case studies presented in the second part of the present article are all based on the existence of the $T_0(r_0)$ relationship. It is therefore rather likely that the trend is a generic physical phenomenon of land surfaces with heterogeneity in hydrological and vegetative conditions. Although research on the synergistic use of multi-spectral measurements has concentrated on the T_0(NDVI) relationship (e.g. Nemani et al., 1993), it will be demonstrated that $T_0(r_0)$ relationships have additional advantages: The slope of the observed $T_0(r_0)$ relationship has a physical meaning which is related to the area-effective momentum flux. The basic equation to demonstrate this is a substitution of the radiation balance into the surface energy balance

$$K^{\downarrow} - r_0 K^{\downarrow} + L^{*} = G_0 + H + \lambda E \qquad (\mathrm{Wm}^{-2}), \quad (16)$$

which after expressing in r_0 yields

$$r_0 = \frac{1}{K^{\downarrow}}(K^{\downarrow} + L^{*} - G_0 - H - \lambda E). \quad (17)$$

Differentiation of Eq. (17) with respect to T_0 gives the regional coupling between r_0 and T_0 and the response of surface fluxes to changes in r_0 and T_0

$$\frac{\partial r_0}{\partial T_0} = \frac{1}{K^{\downarrow}}\left\{\frac{\partial L^{*}}{\partial T_0} - \frac{\partial G_0}{\partial T_0} - \frac{\partial H}{\partial T_0} - \frac{\partial \lambda E}{\partial T_0}\right\}. \quad (18)$$

Surface temperature can only decrease with increasing albedo values if the evaporation process is ruled out. Otherwise T_0 must increase owing to less evaporative cooling. For a set of surface elements or pixels being located on the negative slope between T_0 and r_0 (class 6–8 in Fig. 4B), the conditions $\lambda E \approx 0$, and $\partial \lambda E/\partial T_0 \approx 0$ are fulfilled. If $\partial \lambda E/\partial T_0 \approx 0$, then Eq. (18) turns into

$$\frac{\partial r_0}{\partial T_0} = \frac{1}{K^{\downarrow}}\left\{\frac{\partial L^{*}}{\partial T_0} - \frac{\partial G_0}{\partial T_0} - \frac{\partial H}{\partial T_0}\right\}. \quad (19)$$

The advantage of Eq. (19) is that for dry land elements at the regional scale, $\partial H/\partial T_0$ can be approximated by remote sensing estimates of $\partial r_0/\partial T_0$. The height at which the fluxes apply is a function of the horizontal extent of the surface. The condition $\partial T_{\mathrm{p-B}}/\partial T_0 = 0$ applies at a higher altitude and thus for a regional scale. The potential temperature, $T_{\mathrm{p-B}}$ at the blending height for heat transport, z_{B}, is regionally constant (Claussen, 1990). The value of $\partial H/\partial T_0$ derived from Eq. (19) after solving $\partial L^{*}/\partial T_0$, $\partial G_0/\partial T_0$ and $\partial r_0/\partial T_0$ has a physical meaning which provides the opportunity to obtain $r_{\mathrm{ah-B}}^{\mathrm{dry}}$

$$\frac{\partial H}{\partial T_0} = \frac{\rho_{\mathrm{a}} c_{\mathrm{p}}}{r_{\mathrm{ahB}^{\mathrm{dry}}}} + \rho_{\mathrm{a}} c_{\mathrm{p}} \frac{\partial}{\partial T_0}\left(\frac{1}{r_{\mathrm{ahB}^{\mathrm{dry}}}}\right) T_0 \qquad (\mathrm{Wm}^2\,\mathrm{K}^1). \quad (20)$$

Unfortunately, the second term of the right hand sight of Eq. (20) cannot be solved analytically. A numerical differentiation is, however, feasible when the Monin Obukhov length L is solved at different T_0-values. Therefore, the area-effective buoyancy effect imbedded in $r_{\mathrm{ahB}}^{\mathrm{dry}}$ has to be quantified first. A solution for the stability correction for heat over dry land surface elements, $\psi_{\mathrm{h}}^{\mathrm{dry}}$, requires estimates of the area-effective $\langle H \rangle$ for all pixels on the radiation controlled branch of the $T_0(r_0)$ relationship. Without further field investigations, the negative slope between r_0 and T_0 can be used to distinguish pixels for which it may be assessed that $\lambda E \approx 0$. The area-effective H-value at these dry land surface elements can be obtained by weighted averaging of the distributed H-fluxes under restricted physical conditions (Shuttleworth, 1988)

$$H_{\mathrm{dry}} = -\sum_{n}^{1}(Q^{*} - G_0)x, y \qquad for \partial r_0/\partial T_0 < 0$$

$$(\mathrm{Wm}^{-2}), \quad (21)$$

where n is the number of pixels with $\partial r_0/\partial T_0 < 0$. Hence, the $T_0(r_0)$ relationship provides a unique opportunity without further ground information to retrieve $\partial H/\partial T_0$ and $r_{\mathrm{ahB}}^{\mathrm{dry}}$ from Eq. (20), which after having solved the effective thermal stability correction $\psi_{\mathrm{h}}^{\mathrm{dry}}$ and effective surface roughness length $z_{0\mathrm{h}}^{\mathrm{dry}}$ for dry land surface elements can be used to estimate the area-effective momentum flux, u_{*}^{dry} according to

$$r_{\mathrm{ahB}}^{\mathrm{dry}} = \frac{1}{k u^{*}\mathrm{dry}}\left\{\ln\left(\frac{Z_{\mathrm{B}}}{Z_{0\mathrm{h}}^{\mathrm{dry}}}\right) - \psi_{\mathrm{h}}^{\mathrm{dry}}\right\} \qquad (\mathrm{sm}^{-1}). \quad (22)$$

5.1.1. Area-effective surface roughness length for heat transport, $z_{0\mathrm{h}}^{\mathrm{dry}}$

The effective roughness length $z_{0\mathrm{h}}^{\mathrm{dry}}$ is a value that yields the correct area-effective $< H >$ value by

using boundary layer similarity theory over a given landscape structure and topography. The roughness length for heat transport, z_{0h}, is related to the aerodynamic resistance according to Eq. (22).

In this stage of the computation, z_{0h}^{dry}, ψ_h^{dry} and u_*^{dry} are all unknown. We will first discuss z_{0h}^{dry} then ψ_h^{dry} and determine u_*^{dry} as the left unknown. Noilhan and Lacarrere (1995) used a simple logarithmic averaging procedure for the Hapex–mobilhy area

$$z_{0h}^{eff} = \exp\left\{\frac{1}{n}\left(\sum_{i=1,n} \ln z_{0h}(x,y)\right)\right\} (m), \quad (23)$$

where n represents the number of land surface elements or pixels. The distributed values of roughness length for heat transport at any pixel are computed from the roughness length for momentum transport (Moran, 1990)

$$z_{0m}(x,y) = \exp(c_2 + c_3 NDVI(x,y)) \quad (m), \quad (24)$$

The conversion of $z_{0m}(x,y)$ into $z_{0h}(x,y)$ is done by the kB^{-1} factor ($kB^{-1} = \ln z_{0m}/z_{0h}$). Eq. (24) is essentially meant to describe the roughness effects on surface drag as a function of leaf area development for a particular crop. It does not describe the effect a landscape structure has on z_{0m}. For conditions of natural vegetation with dispersed shrubs and trees, z_{0m} depends on the spacing, shape, size, distribution and density of these obstacles (Lettau, 1969) which obviously cannot be related to NDVI alone. Raupach (1994) though, found encouraging results from simply modelling z_{0m}/h_v fractions as a function of LAI. The c_2 and c_3 coefficients of Eq. (24) depend on the study area, and can be estimated from measurements of the vegetation height h_v, which are especially important at the extremes of NDVI.

5.1.2. Distributed surface roughness length for heat transfer, $z_{0h}(x,y)$

The ratio between z_{0m} and z_{0h} changes with scale and surface type (e.g. Prevot, 1994; Blyth and Dolman, 1995) and a generic solution to this problem is still in its infancy. Although $kB^{-1} = 2.3$ is commonly applied to indicate the physical difference in z_{0m} and z_{0h}, there is evidence that some land cover classes at specific scales may have significantly larger kB^{-1} values (e.g. Beljaars and Holtslag, 1991. Wang (1998) demonstrated that after consistently applying the transfer equations for H in desert–oasis systems, z_{0h}^{eff} to match $\langle H \rangle$ to be larger than z_{0m}^{eff} to match $\langle \tau \rangle$ The latter results in negative kB^{-1} values at a scale of 100 km. Hence, z_{0h} can be derived from z_{0m} under controlled experimental conditions, but the description of the spatial variability of $z_{0h}(x,y)$ in heterogeneous landscapes is not straightforward.

Another problem is that the aerodynamic surface temperature T_{z0h} required to solve H is not equal to the radiometric surface temperature T_0 retrievable from remote sensing data. To circumvent the problem of adjusting z_{0m}/z_{0h} to T_0 (e.g. Sugita and Brutsaert, 1990; Lhomme et al., 1994), it is hereby suggested to adjust $T_{z0h} - T_a$ to z_{0h}. This solution is based on assessing z_{0h} first from spatially variable $z_{0m}(x,y)$ and an areal constant kB^{-1} value (which may give erroneous $z_{0h}(x,y)$ values). The temperature difference between T_{z0h} at height is z_{0h} and T_a at reference height can then be assessed to match a particularly measured or estimated sensible heat flux. By doing so, the need for explicitly quantifying aerodynamic surface temperatures T_{z0h} from T_0 is eliminated because $T_{z0h} - T_a$ is derived from H flux and roughness length z_{0h}. In this approach, the relevant role of kB^{-1} to convert radiometric into aerodynamic surface temperature is reduced and $kB^{-1} = 2.3$ can be satisfactorily used for watersheds. The calculation of $z_{0m}(x,y)$ should, however, be done as accurately as possible as $z_{0m}(x,y)$ is also required for the disaggregation of area-effective momentum flux u_*^{eff} into local scale momentum fluxes, $u_*(x,y)$.

Without u_*^{dry}, neither the Monin–Obukhov length L^{dry}, nor the stability correction ψ_h^{dry} for heterogeneous and dry terrain can be solved. However, u_*^{dry} is imbedded in r_{ah-B}^{dry} and L^{dry} and an iteration is designed to obtain u_*^{dry}. The numerical procedure of Holtslag and Van Ulden (1983) to estimate u_* and update L and $t > it > \psi_h$ with consecutive improvements in $u_*$for a pasture area in The Netherlands is followed. The solution of the iteration yields an area-effective u_*^{dry} value. As the area-effective momentum flux τ^{eff} is approximately similar for wet and dry land surface elements (some differences owing to stability corrections persists), $u_*^{dry} \sim u_*^{eff}$ is a reasonable assumption and τ^{eff} becomes

$$\tau^{eff} \sim \rho_a \left(u_*^{dry}\right)^2 \quad (Nm^{-2}). \quad (25)$$

5.2. Disaggregated momentum flux, $\tau(x,y)$

A disaggregation of τ^{eff} was deemed necessary to estimate local scale momentum fluxes. Anticipating also that, the standard logarithmic wind profile expression is used to infer the area-effective near-surface wind speed at $z = z_{sur}$ using u_*^{eff} and z_{0m}^{eff}

$$u(z_{sur}) = \frac{u_*^{\text{eff}}}{K}\left[ln\left(\frac{z_{sur}}{Z_{0m}^{\text{eff}}}\right) - \psi_m^{\text{eff}}\right] \quad (\text{ms}^{-1}), \quad (26)$$

where k is the von Karman constant and ψ_m is stability correction for momentum transfer. The value for z_{0m}^{eff} is computed in the same manner as was done for z_{0h}^{dry} (see Eq. (23)).

The SEBAL schematisation is based on Fiedler and Panofsky (1972) of a near-surface area-effective wind speed, $u(z_{sur})$, in combination with a local surface roughness, $z_{0m}(x,y)$. For $z < z_{sur}$, u_*^{eff} can be disaggregated into $u_*(x,y)$ using local estimates of terrain roughness as

$$u_*(x,y) = \left\{\frac{1}{ku(z_{sur})}\left[\ln\frac{z_{sur}}{z_{0m}(x,y)} - \psi_{m'}(x,y)\right]\right\}^1 \quad (27)$$

(ms^1).

6. Sensible and latent heat fluxes

At wet surfaces where water vapour is released with a rate determined by the atmospheric demand, the vertical difference in air temperature δT_a is reduced to a minimum. A downward sensible heat flux to the ground arises if evaporation cools the air, a phenomenon known as 'advection entrainment' (McNaughton, 1976). Kalma and Jupp (1990) and Gay and Bernhofer (1991) conducted measurements above wet surfaces under arid conditions, which showed that T_a can exceed T_0 by several degrees during daytime. Except at boundaries between wet and dry surfaces, however, this heat enhancement of λE rarely exceeds the net available energy $(Q^* - G_0)$ by 10%. A general assumption of an evaporative fraction of 100% ($\Lambda = 1.0$) at wet surfaces is therefore a safe first approximation. Sub-areas exhibiting extremes in evaporative fraction can be appraised on the basis of the $T_0(r_0)$ relationship. This makes it feasible to identify specific pixels where $Q^* = H + G_0$ ($\lambda E = 0$) and where pixels with $Q^* = G_0 + \lambda E$ (H = *0*) apply. The challenge of thermal infrared remote sensing is to correctly interpolate the surface energy balance of all other pixels between these two extremes. Appendix C summarizes all necessary computation steps for sensible and latent heat fluxes.

6.1. Distributed air resistance to heat transport, $r_{ahsur}(x,y)$

As $u_*(x,y)$ and $z_{0h}(x,y)$ are solved in this stage of the computations, $r_{ahsur}(x,y)$ can be assessed for any near-surface integration height z_{sur}

$$r_{ah-sur}(x,y) = \frac{1}{ku_*(x,y)}\left\{\ln\left[\frac{z_{sur}}{z_{0h}(x,y)}\right] - \varphi z_{hsur}(x,y)\right\}$$

(ms^1).

(28)

The sensible heat flux $H(x,y)$ is implicitly present in the stability correction, $\psi_{hsur}(x,y)$, which makes the computation of $r_{ahsur}(x,y)$ less straightforward. During the first approximation of $r_{ahsur}(x,y)$, all pixels have $H(x,y) = 0$ (thus $\psi_h = 0$). The latter will yield a first, and wrong, estimate of $H(x,y)$. Using the H-values so obtained in the second iterative loop will give a second estimate of $H(x,y)$ etc. A number of 3–4 iterations is usually sufficient to obtain stationarity in H-fluxes.

6.2. Near-surface vertical air temperature difference, $\delta T_a(x,y)$

Sensible heat flux is traditionally estimated inferring T_{z0h} from remote sensing data (assuming $T_{z0h} = T_0$, after adjusting kB^{-1}) and T_a from synoptic measurements. As T_{z0h} and T_a for each land unit needs to be measured at different elevations and exactly on the same moment and place with a very high degree of precision, the combination of independent T_{z0h} and T_a measurements for estimating δT_a may create severe practical problems. It is therefore easier to estimate δT_a from an inversion of the transfer equation for sensible heat which guarantees reasonable H-fluxes in composite terrain and links kB^{-1} physically to δT_a in a physically and mathematically correct

manner.

$$T_{z0h} - T_a = \delta T_a = \frac{Hr_{ah}}{\rho_a c_p} \qquad \text{(K)}. \tag{29}$$

Values for δT_a are ultimately linked to kB^{-1} (see also Kustas et al., 1989) because T_{z0h} determines $\delta T_a$and z_{0h} affects T_{z0h}. The practical bottleneck of solving Eq. (29) is that H is only known at the extremes of the $T_0(r_0)$ relationship ($H = 0$ and $H = Q^* - G_0$). For these specific land surface elements, δT_a can be solved according to Eq. (29). As surfaces with high δT_a-values coincide with high thermally emitted spectral radiance values, and $\delta T_a = 0$ is linked to a low thermal emission, the radiometric surface temperature T_0 may be used to interpret δT_a across the image. A more detailed investigation of the possibility of using T_0 from Eq. (2) as an interpreter of δT_a in composite terrain is worthwhile. For heterogeneous land surfaces, the following expression is assumed to be valid

$$\delta T_a = c_4 T_0 - c_5 \qquad \text{(K)}, \tag{30}$$

where c_4 and c_5 are the linear regression coefficients valid for one particular moment and landscape. The correctness of Eq. (30) has been investigated using data collected from large scale field experiments held in Niger (Fig. 5), Egypt and China (Wang et al., 1995) (Fig. 6). Franks and Beven (1997) demonstrated also the validity of Eq. (30) for the FIFE study area in Kansas. If the minimum and maximum values of δT_a are calculated for the coldest and warmest pixel(s), the extremes in H are 'anchored' and outliers of H-fluxes will be prevented. The c_4 and c_5 coefficients can be based on pixels with given $H = Q^* - G_0$, δT_a and T_0 values. Moreover, the whole discussion of the accuracy attainable in deriving T_0 from remote sensing measurements becomes less important if δT_a is derived by inversion of H-flux rather than from independent T_0 and T_a measurements and kB^{-1} adjustment. In SEBAL, surface temperature T_0 is only meant to distribute δT_a regionally according to the magnitude of T_0, but does not contribute to the establishment of δT_a.

6.3. Sensible H(x,y) and latent heat flux,λE(x,y)

As the transport resistance $r_{ahsur}(x,y)$ and the driving gradient $\delta T_a(x,y)$ have been mapped, and care was taken that the extremes of H are 'anchored' by adjusting the $\delta T_a(T_0)$ relationship, $H(x,y)$ can be found as

$$H(x,y) = \frac{\rho_a c_p}{r_{ahsur}(x,y)} \delta T_{asur}(x,y) \qquad (\mathrm{Wm}^{-2}). \tag{31}$$

For conditions of zero horizontal advection (which is considered by relating the integration height for flux computations z_{sur} to pixel size), λE can be obtained as the residual of the energy budget theorem

$$\lambda E(x,y) = Q^*(x,y) - G_0(x,y) - H(x,y) \qquad (\mathrm{Wm}^{-2}). \tag{32}$$

7. Summary

Net radiation is obtained from distributed hemispherical surface reflectance and surface temperature data in combination with spatially variable zenith angles to account for variable incoming short wave radiation values. Soil heat flux is obtained from an empirical soil heat flux/net radiation fraction that accounts for the phase difference between soil heat flux and net radiation arising during a daytime cycle. Surface temperature is included in the parameterization for soil heat flux to assess more accurately the large soil heat flux occurring when fractional soil coverage is low. The area-effective momentum flux is computed from the slope between surface albedo and surface temperature rather than from conventional vertical wind profiles or sonic measurements conducted at ground level. The vertical air temperature difference between aerodynamic surface temperature and air temperature is obtained from inversion of the transfer equation for sensible heat flux and linked linearly afterwards to the remotely sensed radiometric surface temperature. It can only be done at wet ($H = 0$) and dry pixels ($\lambda E = 0$). This excludes the need for independent synoptic air temperature observations and ensures a correct physical coupling between the surface roughness for heat transport, vertical temperature gradients and fluxes – which is one of the greatest obstacles in thermal remote sensing (Carlson, 1995). The formulation of the sensible heat flux follows the Monin–Obukhov similarity hypothesis. The latent heat flux is obtained as the residue of the land surface energy balance. The

Table 1
Advantages and disadvantages of the new SEBAL scheme

Advantages	Disadvantages
Minimal collateral data required	Cloud-free conditions required
Physical concept, and therefore applicable for various climates	Presence of drylands ($\Lambda = 0$) and wetlands ($\Lambda = 1$) required
No need for land use classification	Surface roughness is poorly described
No need to involve data demanding hydrology and PBL models	Only suitable for flat terrain.
Possibility to obtain semi-variograms and probability density functions of the most essential hydro-meteorological parameters if high resolution data is used	
Method is suitable for all visible, near-infrared and thermal-infrared radiometers, which implies that it can be applied at different spatial and temporal resolutions (that does not mean that a high accuracy is guaranteed for all combinations of scale and resolution)	
For high resolution images, the results can be verified with in-situ fluxes and soil moisture measurements	
Modular approach.	

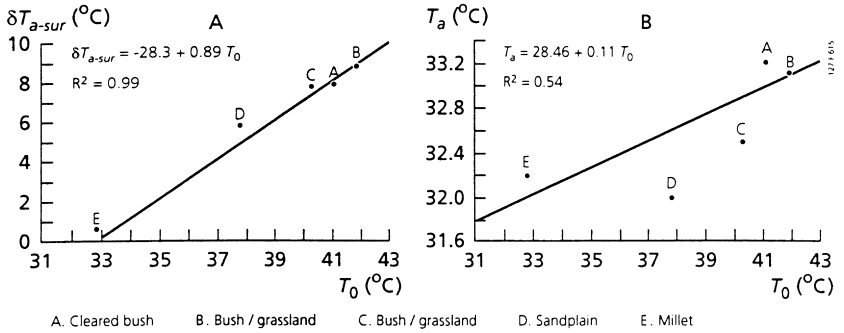

Fig. 5. Linearity of air temperature T_a, near-surface vertical air temperature differences δTa and surface temperature T_0 measured at the West Central Super-site during HAPEX–SAHEL, September 1992, Part A: $\delta T_a(T_0)$ relationship, Part B: $T_a(T_0)$ relationship.

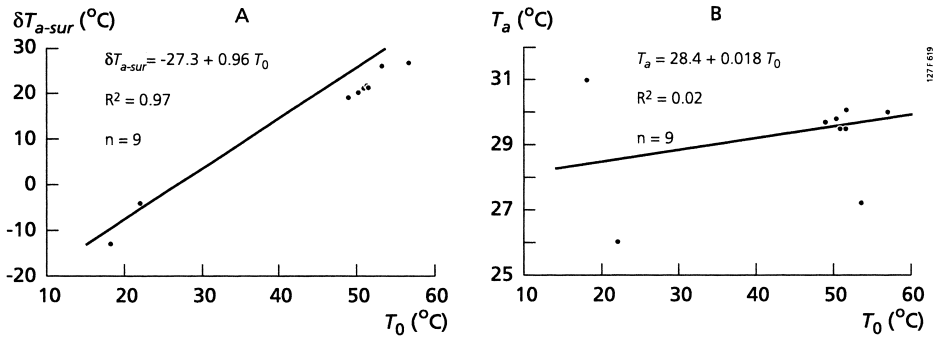

Fig. 6. Observed behaviour of near-surface vertical air temperature differences, $\delta T_{a\text{-}sur}$, and surface temperature, T_0, in the HeiHe basin, China with distinct land surface types such as desert, oases and mountains along a 50 km transect, July 9 1991. (A) $\delta T_{a\text{-}sur}$ (T_0) relationship and (B) $T_a(T_0)$ relationship.

Table 2
Steps in the determination of the surface radiation balance

Computation step	Symbol	Unit	Equation
1.	$K^{\uparrow}_{TOA}(b)$	$Wm^{-2}\ sr^{-1}\ \mu m^{-1}$	$K^{\uparrow}_{TOA}(b)(x,y) = c_{15} + (c_{16} - c_{15})/255\ DN(x,y)$
2.	δ	Rad	$\delta = 0.409 * sin(0.0172\ J - 1.39)$
3.	$omega;_a(x)$	Rad Decimal hours	$(x) = \pi\{t(x) - 12\}/12$ $T(x) = T\ +\ \text{min}/60 + \text{long}\ 12/\pi$
4.	$\phi_{su}(x,y)$	Rad	$\text{Cos}\phi_{su}(x,y) = \sin(\delta)\sin/\{\text{lat}\ (y)\} + \cos(\delta)\cos\{\text{lat}(y)\}\cos\{\omega(x)\}$
5.	d_s	AU	$d_s = 1\ +\ 0.0167\ \sin\ (2\ \pi\ (J\ -\ 93.5))/365$
6.	$K^{\uparrow}_{TOA}(b)$	Wm^{-2}	varies with spectral characteristics of radiometer
7.	$K^{\downarrow}_{TOA}(b)$	Wm^{-2}	$K^{\downarrow}_{TOA}(b) = (K^{\downarrow}_{TOA}(b)\cos(\phi_{su})(x,y))/d^2$
8.	$r_p(b)(x,y)$	—	$r_p(b)(x,y) = \pi K^{\downarrow}_{TOA}(b)/K^{\downarrow}_{TOA}(b)$
9.	$r_p(x,y)$	—	$r_p(x,y) = \int r_p(\lambda)d\lambda = \Sigma c(b)_I r_p(b)_I$
10.	$r_0(x,y)$	—	$r_0(x,y) = (r_p(x,y) - r_a)/\tau''_{sw}$
11.	NDVI (x,y)	—	$\text{NDVI}\ (x,y) = (r_0(\text{IR})(x,y)\ -\ r_0(\text{R})(x,y))/(r_0(\text{IR})(x,y)\ +\ r_0(\text{R})(x,y))$
12.	τ_{sw}	—	$\tau_{sw} = \tau^{0.5}_{sw} = ((r_p(x,y) - r_a)/r_0(x,y))^{0.5}(\text{if}r_0\text{ismeasured})$
13.	$K^{\downarrow}(x,y)$	Wm^{-2}	$K^{\downarrow}(x,y) = K^{\downarrow}_{TOA}(x,y)\tau_{sw}$
14.	ε'_2	—	$\varepsilon'_2\text{avg} = 1.08(-\ \ln\tau^{\text{avg}}_{sw})^{0.265}$
15.	$L^{\downarrow}$	Wm^{-2}	$L^{\downarrow} = \varepsilon'_2\text{avg}\sigma T^{*4}_a$
16.	$\epsilon_0(x,y)$	—	$\epsilon_0(x,y) = 1.009\ +\ 0.047\ \ln\ \text{NDVI}(x,y)$
17.	$T_0(x,y)$	Wm^{-2} K	$L^{\uparrow}_{TOA}(b) = \tau_{lw}L^{\uparrow}(b) + L^{\uparrow}_{alm}(b) + \tau_{lw}(1 - \varepsilon_0)L^{\downarrow}(b)$ $T_0(x,y) = \{[L_\lambda(T_0)^{bh}xy]/c_{16}\}c^{-1}_{17}$
18.	$L^{\uparrow}(x,y)$	Wm^{-2}	$L^{\uparrow}(x,y) = \sigma\varepsilon_0(x,y)T^4_0(x,y)$
19.	$Q^{*}(x,y)$	Wm^{-2}	$Q^{*}(x,y) = K^{\downarrow}(x,y) - r_0(x,y)K^{\downarrow}(x,y) + L^{\downarrow} - ^{\uparrow}(x,y)$
Where			
c_b	Weighing coefficient spectral reflectance's		
d_s	earth-sun distance	AU	
g	Acceleration caused by gravity	ms^{-2}	
h_v	Vegetation height	m	
J	day number		
r_a	Atmospherical reflectance		
$r_p(\lambda)$	spectral planetary reflectance		
T_s	soil temperature	K	
t	local time	h	
t'	GMT time	h	
δ	solar declanation	rad	
σ	Stefan Boltzmann constant	$Wm^{-2}\ K^{-4}$	
τ_{lw}	Atmospheric long wave transmittance		
ϕ_{su}	sun zenith angle	rad	
ω_a	solar hour angle	rad	

advantages and disadvantages are summarized in Table 1.

8. Conclusions

Contrary to the findings of Hall et al. (1992), realistic H-fluxes can be derived from thermal infrared remote sensing measurements. The solution lies essentially in deducing δT_a from a predefined value of kB^{-1} together with H of non-evaporating land surfaces. It is suggested that this has more potential than calibrating kB^{-1} for a unique combination of T_0, T_a and H. This is considered to be an improvement in assessing the spatial variation of H because the spatial variation of $z_{0h}(x,y)$ is much more uncertain than of δT_a. The linear $\delta T_a(T_0)$ hypothesis for heterogeneous terrain conditions is experimentally proven. The advantage to the present approach appears to be the lower demands for input information.

Although the main principals are based on the physics of heat transfer and conservation of energy, empirical relationships were deemed to involve. The empirical relationships between

$$L^{\uparrow}(\mathrm{b})/L^{\uparrow}_{\mathrm{TOA}}(\mathrm{b}), r_0(r_p), \Gamma(T_0, r_0, \mathrm{NDVI}), T_0(r_0), \delta T_a(T_0), \times \varepsilon'(\tau_{sw}), \varepsilon_0(\mathrm{NDVI})$$

and $z_{0m}(\mathrm{NDVI})$ are valid for describing the environmental conditions. The latter does not imply that the coefficients in the relationship are the same for each area, for each acquisition time and for each length scale. The $L^{\uparrow}(\mathrm{b})/L^{\uparrow}_{\mathrm{TOA}}(\mathrm{b})$ and $r_0(r_p)$ relationships vary with atmospheric conditions and need to be tested for each image with pyranometers for $K^{\downarrow}$ and temperature at a few selected synoptic stations. The $\delta T_a(T_0)$ relationship is automatically adjusted, as it is part of the H-inversion scheme. A thorough sensitivity analysis has been performed (Bastiaanssen, 1995), revealing that the fluxes are insensitive to the empirical equations with regression coefficients which do not change, i.e. the $\Gamma(r_0, T_0, \mathrm{NDVI})$, $\epsilon'(\tau_{sw})$ and $\epsilon_0(\mathrm{NDVI})$ relationships. The price to pay for this new approach is the dependence on the correctness of empirical relationships. Experiences gained during the last 5 y are, however, encouraging. Paper 2 demonstrates the accuracies attainable with SEBAL in relation to scale.

Acknowledgements

The authors are indebted to Mrs. Mieke van Dijk for her skilful help in preparing the electronic manuscript. The assistance of Mr. Bram ten Cate in the organisation of the final editing is acknowledged. The helping hand of Dr. Jim Lenahan of the International Water Management Institute at Colombo, (Sri Lanka) is respectfully appreciated.

Table 3
Steps in the determination of the momentum flux

Computation step	Symbol	Unit	Expression
1.	$z_{0m}(x,y)$	M	$z_{0m}(x,y) = \exp(c_2 + c_3\mathrm{NDVI}(x,y))$
2.	$z_{0h}(x,y)$	M	$z_{0h}(x,y) = z_{0m}(x,y)/\exp kB^{-1}$
3.	z_{0h}^{eff}	M	$z_{0h}^{\mathrm{eff}} = \exp\{\ln z_{0h}(x,y)/n\}$
4.	$\partial L^*/\partial T_0$	$\mathrm{Wm^{-2}\,K^{-1}}$	$\partial L^*/\partial T_0 = -4\varepsilon_0^{\mathrm{dry}}\sigma T_0^{\mathrm{dry3}}$
5.	$\partial G_0/\partial T_0$	$\mathrm{Wm^{-2}\,K^{-1}}$	$G_0 = c_4 + c_3 T_0$
6.	$\partial r_0/\partial T_0$	$\mathrm{K^{-1}}$	$T_0 = c_6 + c_7 r_0$
7.	$r_{at.}^{\mathrm{Bdry}}$	$\mathrm{sm^{-1}}$	$r_{ah.}^{\mathrm{Bdry}} = f(\partial H/\partial T_0, H^{\mathrm{dry}}, T_0^{\mathrm{dry}})$
8.	H^{dry}	$\mathrm{Wm^{-2}}$	$H^{dry} = \{\Sigma(Q^*(x,y)G_0(x,y))\}/n$
9.	L^{dry}	m	$L^{\mathrm{dry}} = (\rho_a c_p u_*^{\mathrm{dry3}} T^{\mathrm{dry}})/(\mathrm{kg}H^{\mathrm{dry}})$
10.	$u_{\mathrm{sur}}^{\mathrm{eff}}$	$\mathrm{ms^{-1}}$	$u_{\mathrm{sur}}^{\mathrm{eff}} = (\ln z_B/z_{0m}^{\mathrm{dry}} - \psi_0^{\mathrm{dry}})u^{*\mathrm{dry}}/k$
11.	$u_*(x,y)$	$\mathrm{ms^{-1}}$	$u^*(x,y) = \{\ln z_{\mathrm{sur}}/z_{0m}(x,y) - \psi^{ku_{\mathrm{sur}}^{\mathrm{eff}}}\}$
12.	τ	$\mathrm{Nm^{-2}}$	$\tau(x,y) = \rho_a u_*^2$

Table 4
Steps in the determination of the sensible and latent flux

Computation step	Symbol	Unit	Expression
1.	$r_{ahsur}(x,y)$	sm^{-1}	$r_{ahsur}(x,y) = \{\ln z_{sur}/z_{0h}(x,y)\text{-}\psi_{h-sur}(x,y)\}/\{ku_*(x,y)\}$
2.	$\delta T_a(x,y)$	°C	$\delta T_a(x,y) = c_4 T_0(x,y) - c_5$
3.	$H(x,y)$	Wm^{-2}	$H(x,y) = \rho_a c_p \delta T_a(x,y)/r_{ahsur}(x,y)$
4.	$L(x,y)$	m	$L(x,y) = [\rho_a c_p u_*(x,y)^3 T_0]/[kgH(x,y)]$
5.	$\lambda E\ (x,y)$	Wm^{-2}	$\lambda E\ (x,y) = Q^*(x,y) - G_0(x,y) - H\ (x,y)$

Appendix A. Net radiation calculation scheme

Table 2

Appendix B. Momentum flux calculation scheme

Table 3

Appendix C. Sensible heat flux calculation scheme

Table 4

References

Bastiaanssen, W.G.M., 1995. Regionalization of surface flux densities and moisture indicators in composite terrain, Ph.D. thesis, Agricultural University, Wageningen, The Netherlands, p. 288.

Bastiaanssen, W.G.M., 1998. Remote sensing in water resources management: the state of the art, International Water Management Institute, Colombo, Sri Lanka, p. 118.

Beljaars, A.C.M., Holtslag, A.A.M., 1991. Flux parameterization over land surfaces for atmospheric models. J. of Applied Met. 30 (3), 327–341.

Blyth, E.M., Dolman, A.J., 1995. The roughness length for heat of sparse vegetation. J. of Applied Met. 34, 583–585.

Bouman, B.A.M., van Keulen, H., van Laar, H.H., Rabbinge, R., 1996. The school of de Wit crop growth simulation models: a pedigree and historical overview. Agricultural Systems 52 (2/3), 171–198.

Brutsaert, W., Hsu, A.Y., Schmugge, T.J., 1993. Parameterization of surface heat fluxes above forest with satellite thermal sensing and boundary layer soundings. J. of Applied Met. 32 (5), 909–917.

Carlson, T.N., Taconet, O., Vidal, A., Gilles, R.R., Olioso, A., Humes, K., 1995. An overview of the workshop on thermal remote sensing, held at La Londe les Maures. Agr. and Forest Met. 77 (3/4), 141–152.

Chen, T.S., Ohring, G., 1984. On the relationship between clear sky planetary and surface albedos. J. Atmos. Science 41, 156–158.

Choudhury, B.J., Idso, S.B., Reginato, R.J., 1984. Analysis of an empirical model for soil heat flux under a growing wheat crop for estimating evaporation by an infrared-temperature based energy balance equation. Agr. and Forest Met. 39, 283–297.

Choudhury, B.J., 1989. Estimating evaporation and carbon assimilation using infrared temperature data. In: Asrar, G. (Eds.), Vistas in modeling, in Theory and Applications of Optical Remote Sensing. Wiley, New York, pp. 628–690.

Choudhury, B.J., DiGirolamo, N.E., 1998. A biophysical process-based estimate of global land surface evaporation using satellite and ancillary data, 1 model description and comparison with observations. J. of Hydr. 205, 164–185.

Claussen, M., 1990. Area-averaging of surface fluxes in a neutrally stratified, horizontally inhomogeneous atmospheric boundary layer. Atmospheric Environment A24 (6), 1349–1360.

Clothier, B.E., Clawson, K.L., Pinter, P.J., Moran, M.S., Reginato, R.J., Jackson, R.D., 1986. Estimation of soil heat flux from net radiation during the growth of alfalfa. Agr. and Forest Met. 37, 319–329.

Daughtry, C.S.T., Kustas, W.P., Moran, M.S., Pinter, P.J., Jackson, R.D., Brown, P.W., Nichols, W.D., Gay, L.W., 1990. Spectral estimates of net radiation and soil heat flux. Rem. Sens. Envir. 32, 111–124.

Famigliette, J., Wood, E.F., 1994. Application of multiscale water and energy balance models on a tall grass prairi. Water Resources Research 30, 3079–3093.

Fiedler, F., Panofsky, H.A., 1972. The geostrophic drag coefficient and the effective roughness length. Q. J. R. Met. Soc. 98, 213–220.

Gay, L.W., Ch. Bernhofer, 1991. Enhancement of evapotranspiration by advection in arid regions. In: Kienitz et al. (Eds.), Hydrological interactions between atmosphere, soil and vegetatation. Proc. Vienna conference, vol. 204. IAHS Publication, pp. 147–156.

van de Griend, A.A., Owe, M., 1992. On the relationship between thermal emissivity and the normalized difference vegetation index for natural surfaces. Int. J. of Rem. Sensing 14 (6), 1119–1131.

Hall, F.G., Huemmrich, K.F., Goetz, S.J., Sellers, P.J., Nickeson, J.E., 1992. Satellite remote sensing of surface energy balance: success failures and unresolved issues in FIFE. J. of Geophysical Research 97 D17, 19061–19089.

Holtslag, A.A.M., van Ulden, A.P., 1983. A simple-scheme for daytime estimates of the surface fluxes from routine weather data. J. of Climate and Applied Met. 22 (4), 517–529.

Jackson, R.D., Reginato, R.J., Idso, S.B., 1977. Wheat canopy temperatures: A practical tool for evaluating water requirements. Water Res. Res 13, 651–656.

Kalma, J.D., Jupp, D.L.B., 1990. Estimating evaporation from pasture using infrared thermometry: evaluation of a one-layer resistance model. Agr. and Forest Meteorology 51, 223–246.

Kite, G.W., Dalton, A., Dion, K., 1994. Simulation of streamflow in a macroscale watershed using general circulation model data. Water Resources Research 30 (5), 1547–1559.

Koepke, P., Kriebel, K.T., Dietrich, B., 1985. The effect of surface reflection and of atmospheric parameters on the shortwave radiation budget. Adv. Space Research 5, 351–354.

Kustas, W.P., Choudhury, B.J., Moran, M.S., Reginato, R.J., Jackson, R.D., Gay, L.W., Weaver, H.L, 1989. Determination of sensible heat flux over sparse canopy using thermal infrared data. Agr. and Forest Met. 44, 197–216.

Kustas, W.P., Daughtry, C.S.T., 1990. Estimation of the soil heat flux/net radiation ratio from spectral data. Agr. Forest Met. 49, 205–223.

Kustas, W.P., Norman, J.M., 1996. Use of remote sensing for evapotranspiration monitoring over land surfaces. J. of Hydrological Sciences 41 (4), 495–516.

Lettau, H., 1969. Note on aerodynamic roughness-parameter estimation on the basis of roughness element description. J. of Applied Meteorology 8, 828–832.

Lhomme, J.P., Monteny, B., Amadou, M., 1994. Estimating sensible heat flux from radiometric temperature over sparse millet. Agr. and Forest Met. 68, 77–91.

McNaughton, K., 1976. Evaporation and advection II. Evaporation downwind of a boundary separating regions having different surface resistances and available energies. Q. J. R. Met. Soc. 102, 193–202.

Menenti, M., Bastiaanssen, W.G.M., van Eick, D., Abd El Karim, M.H., 1989. Linear relationships between surface reflectance and temperature and their application to map actual evaporation of groundwater. Advances in Space Research 9 (1), 165–176.

Menenti, M., 1993. Understanding land surface evapotranspiration with satellite multispectral measurements. Adv. in Space Research COSPAR 13 (5), 89–100.

Moran, M.S., 1990. A satellite-based approach for evaluation of the spatial distribution of evapotranspiration from agricultural lands. Ph.D. thesis, University of Arizona, Tucson, USA.

Moran, M.S., Jackson, R.D., 1991. Assessing the spatial distribution of evapotranspiration using remotely sensed inputs. J. Envirnm. Qual. 20, 525–737.

Moran, M.S., Humes, K.S., Pinter, P.J., 1997. The scaling characteristics of remotely-sensed variables for sparsely-vegetated heterogeneous landscapes. J. of Hydr. 190, 337–362.

Nemani, R.R., Pierce, L., Running, S.W., Goward, S., 1993. Developing satellite-derived estimates of surface moisture stress. J. Applied Met. 32, 548–557.

Nieuwenhuis, G.J.A., Smidt, E.H., Thunissen, H.A.M., 1985. Estimation of regional evapotranspiration of arable crops from thermal infrared images. Int. J. of Remote Sensing 6, 1319–1334.

Noilhan, J., Lacarrere, P., 1995. GCM gridscale evaporation from macroscale modeling. J. of Climate 8, 206–223.

Norman, J.M., Becker, F., 1995. Terminology in thermal infrared remote sensing of natural surfaces. Agr. and Forest Meteorology 77, 153–166.

Oevelen, van, P.J., 1991. Determination of the available energy for evapotranspiration with remote sensing, M.Sc. Thesis, Agricultural University of Wageningen, p. 68.

Pelgrum, H., Bastiaanssen, W.G.M., 1996. An intercomparison of techniques to determine the area-averaged latent heat flux from individual in situ observations: A remote sensing approach using EFEDA data. Water Resources Research 32 (9), 2775–2786.

Prevot, L, Brunet, Y., Pawll, K.T., Seguin, B., 1994. Canopy modelling for estimating sensible heat flux from thermal infrared measurements, Proc. Workshop on thermal remote sensing, La Londe les Maures, France, 20–23 September, 1993, pp. 17–22.

Raupach, M.R., 1994. Simplified expressions for vegetation roughness length and zero-plane displacement as functions of canopy height and area index. Boundary-Layer Meteorology 71, 211–216.

Rosema, A., Fiselier, J.L., 1990. Meteosat-based evapotranspiration and thermal inertia mapping for monitoring transgression in the Lake Chad region and Niger Delta. Int. J. of Rem. Sens. 11 (5), 741–752.

Schmugge, Becker, 1991. Remote sensing observations for the monitoring of land surface fluxes and water budgets. In Schmugge and Andre (Eds.), Land surface evaporation, measurement and parameterization, pp. 337–347.

Seguin, B., Assad, E., Freteaud, J.P., Imbernon, J.P., Kerr, Y., Lagouarde, J.P., 1989. Use of meteorological satellites for water balance monitoring in Sahelian regions. Int. J. of Rem. Sens. 10, 1101–1117.

Sellers, P.J., Randall, D.A., Collatz, G.J., Berry, J.A., Field, C.B., Dazlich, D.A., Zhang, C., Collelo, G.D., Bounoua, L., 1996. A revised land surface parameterization (SiB2) for atmospheric GCMs part 1: model formulation. J. of Climate 9, 676–705.

Shuttleworth, W.J., 1988. Macrohydrology the new challenges for process hydrology. J. of Hydr. 100, 31–56.

Sucksdorff, Y., Ottle, C., 1990. Application of satellite remote sensing to estimate areal evapotranspiration over a watershed. J. of Hydr. 121, 321–333.

Sugita, M., Brutsaert, W., 1990. Regional surface fluxes from remotely sensed skin temperature and lower boundary layer measurements. Water Resources Research 26 (12), 2937–2944.

Taconet, O., Bernard, R., Vidal-Madjar, O., 1986. Evapotranspiration over an agricultural region using a surface flux temperature model based on NOAA-AVHRR data. J. of Climate and Applied Met. 25, 284–307.

Taylor, C.M., Harding, R.J., Thorpe, A.J., Bessemoulin, P., 1997. A meso scale simulation of land surface heterogeneity from HAPEX-Sahel. J. of Hydr. 188–189, 1040–1066.

Troufleau, D., Lhomme, J.P., Monteny, B., Vidal, A., 1997. Sensible heat flux and radiometric surface temperature over sparse Sahelian vegetation I. An experimental analysis of the kB-1 parameter. J. of Hydr. 188–189, 815–838.

Wang, J., Ma, Y., Menenti, M., Bastiaanssen, W.G.M., Mitsuta, Y., 1995. The scaling-up of processes in the heterogeneous landscape of HEIFE with the aid of satellite remote sensing. J. Met. Soc. of Japan 73 (6), 1235–1244.

Wang, J., Bastiaanssen, W.G.M., Ma, Y., Menenti, M., 1998. Aggregation of land surface parameters in the oasis-desert systems of Northwest China, Hydrological Processes (accepted BAHC and LUCC special issue).